

1 Revision 1

2

Word count: 6676

3 **Hydrogen Solubility in FeSi Alloy Phases at High Pressures and Temperatures**

4 Suyu Fu^{1*}, Stella Chariton², Vitali B. Prakapenka², Andrew Chizmeshya³, Sang-Heon Shim^{1*}

5 ¹School of Earth and Space Exploration, Arizona State University, Tempe, Arizona, USA.

6 ²Center for Advanced Radiation Sources, University of Chicago, Chicago, Illinois, USA.

7 ³School of Molecular Sciences, Arizona State University, Tempe, Arizona, USA.

8 *Corresponding authors: suyufu@asu.edu, sshim5@asu.edu

9

10

ABSTRACT

11 Light elements alloying with metallic Fe can change the properties and therefore play a key
12 role in the structure and dynamics of planetary cores. Hydrogen and silicon are possible light
13 elements in the rocky planets' cores. However, hydrogen storage in Fe-Si alloy systems remains
14 unclear at high pressures and high temperatures because of experimental difficulties. Taking
15 advantage of pulsed laser heating combined with high-energy synchrotron X-ray diffraction, we
16 studied reactions between FeSi and H in laser-heated diamond anvil cells (LHDACs) up to 61.9
17 GPa and 3500 K. We found that under H-saturated conditions the amount of H alloying with
18 FeSi (0.3 and <0.1 wt% for the B20 and B2 structures, respectively) is much smaller than that in
19 pure Fe metal (>1.8 wt%). Our experiments also suggest that H remains in the crystal structure of
20 FeSi alloy when recovered to 1 bar. Further density functional theory (DFT) calculations indicate
21 that the low H solubility likely results from the highly distorted interstitial sites in the B20 and

22 B2 structures which are not favorable for H incorporation. The recovery of H in the B20 FeSi
23 crystal structure at ambient conditions could open up possibilities to understand geochemical
24 behaviors of H during core formation in future experiments. The low H content in FeSi alloys
25 suggest that if a planetary core is Si rich, Si can limit the ingassing of H into the Fe-rich core.

26 **Key words:** FeSi alloy; hydrogen content; planetary cores; pulsed-laser heating; synchrotron
27 X-ray diffraction.

28 INTRODUCTION

29 In recent decades, finding habitable planets has drawn interest from not only astrobiologists
30 and astrophysicists but also Earth scientists. Studies indicate that in addition to atmosphere and
31 surface conditions, the interior of a planet could play a key role for its habitability (Shahar et al.,
32 2019). For instance, the dynamo generated by the core would affect the habitability of the surface
33 environment. Light elements are believed to partition into the Fe metal core during the early
34 magma ocean stage of planets (Stevenson, 2003) and can greatly affect the properties, such as
35 phase relation and melting behavior (Hirose et al., 2013). Considering the diverse sizes and
36 masses of planets found in the solar system and the exo-planetary systems (Batalha et al., 2011;
37 Jontof-Hutter et al., 2015), from Mars-size rocky planets to gas giants, it is key to studying Fe
38 with light elements for a wide range of pressures.

39 Hydrogen is the most abundant element in the universe (Anders and Grevesse, 1989;
40 Grevesse and Sauval, 1998). A large amount of H, more than 1.8 wt%, can be dissolved into
41 solid Fe metal at high pressures (Badding et al., 1991; P'epin et al., 2017). Sakamaki et al. (2009)
42 showed that alloying with H can lower the melting temperature of Fe by as much as 600–900 K
43 below 20 GPa. In some models, Si is thought to be the most abundant light element in the Earth's
44 core, up to 12 wt% (Li and Fei, 2003; Hirose et al., 2013). Based on the S/Si ratio and the FeO

45 content of Mercury's surface, its core could contain more than 12 wt% Si (Nittler et al., 2011;
46 Knibbe and van Westrenen, 2018). Therefore, it is important to include Si in Fe metal for
47 understanding the impact of H on the constituent phases of the planetary cores.

48 Studies on the H content in the Fe–Si system are limited to low pressures and/or low
49 temperatures. For instance, Tagawa et al. (2016) conducted laser heating on $\text{Fe}_{0.88}\text{Si}_{0.12}$ (6.5 wt%
50 Si) in a H medium at 27 and 62 GPa using DACs, and found that about 1.2–1.5 wt% H can be
51 incorporated into the hexagonal-close-packed (hcp) alloy. However, the heating was conducted
52 below ~1000 K. In addition, a multi-anvil experiment reported a much lower H solubility of 0.2–
53 0.3 wt% in the B20-structured FeSi alloys up to 20 GPa and 2000 K (Terasaki et al., 2011).
54 While the pressure is not sufficiently high for rocky planets' cores greater than that of Mars.

55 Despite the importance, studying H in LHDACs has been difficult, because of its fast
56 diffusion into diamond anvils, which can make them brittle. The embrittlement problem becomes
57 more severe with heating. Recently, pulsed laser heating combined with gated synchrotron X-ray
58 diffraction (XRD) enabled heating of H to thousands of kelvins in LHDACs (Goncharov et al.,
59 2010). By taking advantage of the development, we have studied reactions between H and FeSi
60 alloy phases in a H-saturated condition up to 61.9 GPa and 3500 K. We have also conducted
61 density functional theory (DFT) calculation to understand the H incorporation mechanism in the
62 FeSi phases and the impact of H on the seismic properties of the Fe-Si alloy phases. Our study on
63 the H content in FeSi provides essential data for understanding the Si-rich cores of some rocky
64 planets. The data can also serve as a benchmark for future studies on H solubility in low-Si Fe-Si
65 alloys.

66

EXPERIMENTAL METHODS

67 FeSi powders was purchased from Goodfellow Corporation. Symmetric DACs with culet
68 sizes of 150–300 μm beveled and 200 μm flat were used. Re gaskets were pre-indented and holes
69 with diameters of 2/3 of the culet sizes were drilled as sample chambers. Prepared gaskets were
70 coated with gold (>80 \AA thick) to prevent diffusion of H into Re gaskets forming Re hydrides at
71 high P - T . The coating prevents gasket embrittlement by H, which can fail the experiment. The
72 sample was cold pressed into 5–10 μm thick foils using a pair of 400 μm culet diamonds, and
73 then was loaded into the prepared sample chambers. The malleable alloy foil becomes thinner
74 with compression in DAC, likely less than 5 μm . Small pieces of the same starting materials were
75 placed on both sides of the foil to avoid direct contacts between the sample foil and diamond
76 anvils and therefore provide better thermal insulation and laser coupling during heating (Figure
77 1a). A piece of gold was placed close to the foil, as a pressure calibrant (Ye et al., 2018). This
78 pressure scale (Ye et al., 2018), was compared and shown to be consistent with other commonly
79 used pressure calibrants, such as MgO, Pt, and B2 NaCl. Pressures and their uncertainties were
80 determined by measuring the unit-cell volume of Au before and after each high P - T experiment.
81 Pure hydrogen gas was loaded into the DACs as a pressure medium and H source using a gas
82 loading system at Arizona State University. A small ruby chip was put at the edge of the sample
83 chamber to monitor its pressure during gas loading (Figure 1).

84 Laser heating on the high-pressure samples was conducted at 13-IDD beamline of
85 GeoSoilEnviroCARS (GSECARS) of the Advanced Photon Source (APS), Argonne National
86 Laboratory (ANL). The pulsed laser heating system at the beamline is equipped with a 1064-nm
87 wavelength infrared laser with a flat-top spot size of around 10 μm in diameter (Goncharov et al.,
88 2010). We accumulated 100,000 laser pulses of 1 μs width at a rate of 10 kHz, which totals to 10-s

89 accumulation time (including time between pulses) with a ~ 0.1 -s high temperature period for each
90 shot. At least ten shots were repeated to allow for a total heating duration of more than 1 s.
91 Considering that H can easily diffuse into metals, $\sim 10^3 \mu\text{m}^2/\text{s}$ even at low P - T (Zhang et al., 2008)
92 and the grain size of FeSi powder is $\leq 1 \mu\text{m}$, our experimental setup provides sufficient conditions
93 for the sample to fully react with H and possibly to reach the maximum H content. We note that
94 recent experiments used the exact same setups and observed extensive reactions of Fe-S alloys with
95 H (Piet et al., 2021). This shows the effectiveness of the pulsed laser heating to drive chemical
96 reactions between metal alloys and H medium.

97 Double-sided pulsed laser-heating was conducted on the sample in DACs. Temperatures of
98 both sides were calculated by fitting collected thermal radiation spectra between 670 to 840 nm
99 to a Plank function based on a gray-body approximation. Decompression XRD patterns were
100 collected from 46.1 and 61.9 GPa in two runs. To ensure the reaction between the sample and H,
101 we examined the optical changes in the heated area and conducted 2D XRD and chemical
102 mappings (Figures 1-3). XRD measurements were performed using an incident X-ray beam with
103 a wavelength of 0.3344 \AA . We used the PeakPo software for peak identifications and unit-cell
104 fittings (Shim, 2017). The recovered samples were analyzed for chemical compositions and
105 mappings using an Electron Probe Micro Analyzer at the Eyring Materials Center of Arizona
106 State University. A JEOL JXA-8530F electron microprobe operated at an accelerating voltage of
107 15V and a beam current of 20nA.

108

109 **DENSITY FUNCTIONAL THEORY CALCULATIONS**

110 We conducted complementary DFT calculations using the projector augmented-wave (PAW)
111 method with the GPAW package (Blochl, 1994; Mortensen et al., 2005). The approach

112 combined pseudo-potentials, a plane wave description and all-electron calculations in the frozen
113 core approximation to generate smooth valence wave functions (Mortensen et al., 2005). Both the
114 Perdew-Burke-Ernzerhof (PBE) version of generalized gradient approximation (GGA) (Perdew
115 et al., 1996) and Ceperley-Alder (CA) version of local-density approximation (LDA) (Ceperley
116 and Alder, 1980) were used to carry out simulations on each phase. Convergence tests were
117 conducted for proper plane-wave kinetic energy cutoff and Monkhorst-Pack k -point grid density
118 (Table S1). Convergence was achieved when the maximum total force on all individual atoms
119 falls below 0.005 or 0.01 eV/°Å, which allows for optimization of cell shape and internal atomic
120 positions. Static compression equations of state (EoS) were calculated up to 200 GPa with a 10-
121 GPa interval. The pressure-volume data were fit to the 3rd order Birch-Murnaghan (BM) EoS to
122 obtain bulk modulus and its derivative (Table S2). We conducted several tests on H-free FeSi to
123 compare with literature DFT calculations (Caracas and Wentzcovitch, 2004; Zhao et al., 2011;
124 Vocadlo et al., 1999; Moroni et al., 1999). Our GGA results on the unit-cell volumes of both B20
125 and B2 FeSi are consistent with the literature (Figure S1 and Table S1) (Caracas and
126 Wentzcovitch, 2004; Zhao et al., 2011). Our LDA predicts slightly higher unit-cell volumes for
127 B2 FeSi than LDA results by Caracas and Wentzcovitch (2004), but comparable to the
128 calculation by Moroni et al. (1999). Considering the overall consistency of the GGA calculation
129 with our experimental data on FeSi alloy phases (Fischer et al., 2014; Sata et al., 2010; Lin et al.,
130 2003), we will mainly discuss the GGA results.

131 **RESULTS AND DISCUSSION**

132 The FeSi alloy has the B20 structure at ambient conditions (Al-Sharif et al., 2001). XRD
133 patterns show that the B20 structure starts to convert to a B20 + B2 mixture with heating in H at
134 ~20 GPa and ~2400 K (Figure 4). The coexistence of B20 and B2 was also found in H-free FeSi

135 below 42 GPa (Fischer et al., 2013), which could satisfy the Gibbs phase rule (Smith, 1950). In a
136 H medium, the B20 + B2 mixture completely transforms into pure B2 when heated to 1600–2100
137 K at 53.0 GPa.

138 We carefully controlled several important experimental parameters to ensure sufficient
139 reactions between FeSi alloys and H at high *P-T*. Changes from smooth Debye rings to spotty
140 rings in 2D images and sharpening of the diffraction lines in 1D patterns confirm sufficient
141 heating of the sample (Figures 4 and S2). The line positions shift to lower diffraction angles
142 during laser heating. Such peak shifts remain after temperature quenched to 300 K, indicating the
143 unit-cell volume change and possible incorporation of H into the structure (Figure S3). We
144 repeated heating shots (>10) until the unit-cell volume of the synthesized products did not
145 change after heating so that the H content possibly reaches the maximum at the given *P-T*. After
146 heating, we conducted 2D XRD mapping, which shows a small difference (0.4%) in the unit-cell
147 volumes of the synthesized products across the heated area (Figure 2). Chemical maps from
148 EPMA of the recovered samples show that Fe/Si ratio did not change in the heated region (Figure
149 3). These indicate the reaction products between FeSi alloys and H should be homogeneous
150 without additional phases.

151 High-quality XRD patterns of the unheated and the heated samples at high pressure and room
152 temperature allow us to obtain precise lattice parameters of the B20 and B2 phases (Figures 5 and
153 S3; Table 1). The unit-cell volumes of the unheated region are consistent with those reported for
154 H-free B20 FeSi up to 73 GPa within uncertainties (Fischer et al., 2014; Lin et al., 2003),
155 indicating that the FeSi might not react with H at room temperature (solid black circles in Figure
156 5). From the agreement, we can also infer a small pressure gradient (<1 GPa) in the sample
157 chamber, likely owing to the compressible H medium. The observed behavior of FeSi is different

158 from pure metallic Fe, which can react with H to form dhcp FeH with expanded volumes even
159 without heating at 300 K (Badding et al., 1991).

160 With heating up to 2500 K at 20 GPa (Figure 5a-b), the B20 phase shows a <1% greater
161 volume than H-free B20 FeSi. The volume expansion increases up to 4–5% ($0.4 \text{ \AA}^3/\text{Atoms}$)
162 upon more heating runs at 30.1, 42.6, and 46.1 GPa. We note that these unit-cell volumes were
163 collected after heating at 300 K, and H medium provides low deviatoric stress. Therefore,
164 thermal pressure or pressure gradient cannot explain the observed volume expansion in the
165 synthesized phases.

166 One of the most notable observations is that the unit-cell volume of B20 FeSiH_x remains
167 expanded even after pressure quenching to 1 bar with a lattice parameter of $a = 4.5234(4) \text{ \AA}$
168 (Figure 4b) compared to $a = 4.4881(5) \text{ \AA}$ for the unheated sample (Table 1). This observation
169 suggests that H remains in the crystal structure of the B20 phase, which is in contrast with the
170 case of pure Fe metal where the high-pressure dhcp FeH phase converts back to a H-free body-
171 centered cubic (bcc) Fe phase upon decompression to 1 bar (Okuchi, 1997; Badding et al., 1991).
172 We note that at 1 bar the unit-cell volume of the unheated sample is consistent with that of H-free
173 B20 FeSi reported in the literature (Fischer et al., 2014), supporting minimal residual pressure.
174 We also observed optical interference fringes between diamond anvil surface and gasket surface,
175 suggesting a gap which vented H medium and released pressure to 1 bar.

176 Studies have shown that when H is incorporated into pure Fe metal, H would prefer to occupy
177 the octahedral (and possibly tetrahedral) interstitial sites in the face-centered cubic (fcc) or hcp
178 crystal structures to form FeH_x with expanded volumes (Badding et al., 1991; Kato et al., 2020).
179 Accordingly, H contents in the alloys could be estimated empirically using: $x = (V_{\text{MH}_x} - V_{\text{M}})/\Delta V_{\text{H}}$,
180 where ΔV_{H} , V_{MH_x} , and V_{M} are the volume increase per H atom, and the volumes of metal hydride

181 and H-free metal, respectively (Fukai, 1992). Our observed volume expansion in the B20 phase
182 is much smaller than FeH_x alloys (Figure 6) (Badding et al., 1991; Kato et al., 2020). The ΔV_H
183 value is not known for B20 FeSi. If we use an average value of $\sim 2.5 \text{ }^\circ\text{A}^3/\text{Atoms}$ from literature
184 constraints on transition metals and alloys (Fukai, 1992; Machida et al., 2014; Terasaki et al.,
185 2011), the maximum x in our B20 FeSiH_x is approximately 0.17. This value is comparable to that
186 reported in B20 FeSiH_x synthesized in multi-anvil experiments at low pressures ($< 20 \text{ GPa}$),
187 where x is estimated to be 0.07–0.22 (Terasaki et al., 2011). However, the FeSi alloys do not
188 have the close-packed structure, and thus the volume expansion by H in FeSi may be different
189 from those in the close-packed FeH_x phases. We then conducted DFT calculations to gain further
190 insights on the H incorporation mechanism in FeSi alloys as well as its effect on the physical
191 properties.

192 For a B20 crystal structure, an interstitial site exists at the cubic center which can be occupied
193 by a H atom (Figure 5e). This interstitial site is surrounded by 4Fe and 4Si atoms (forming
194 tetrahedra independently) with an 8-fold coordination. From the ratio between the interstitial sites
195 and metal atoms (Fe and Si), x in B20 FeSiH_x can range between 0 and 1. We conducted DFT
196 calculations on B20 FeSiH and B20 FeSiH_{0.25}, where all and a quarter of the cubic-center
197 interstitial sites in a unit cell are occupied, respectively (Figures 5e and S4a). We found the best
198 match between DFT results on the cubic B20 FeSiH_{0.25} and our experimentally measured unit-
199 cell volumes (Figure 5a-b). The H content is also comparable to our empirical estimations. It
200 should be noted that our DFT calculation was conducted in the static lattice approximation, while
201 the unit-cell volume was measured at 300 K in experiments. We then compared the value of V
202 (FeSiH_{0.25}) – V (FeSi) between experiments and DFT (Figure 5b). This approach reduces (or
203 cancels out) the thermal effect, assuming that the thermal behavior of B20 FeSiH_{0.25} is similar to

204 that of B20 FeSi. Also, there are other factors to be considered, such as limitations of DFT
205 calculations and experimental uncertainties.

206 In contrast to the case of the B20 phase, below 46.1 GPa the B2 phase synthesized under H-
207 saturated conditions shows unit-cell volumes consistent with those of the H-free B2 FeSi (Fischer
208 et al., 2014; Sata et al., 2010). After the complete transformation from the B20 + B2 mixture into
209 the B2 phase above 53.0 GPa, we noticed a slight volume decrease for the B2 phase, less than 0.2
210 °A³/Atoms with respect to the H-free case (Figure 5c-d). The volume decrease is about 2%,
211 greater than the estimated uncertainties. The unit-cell volume decrease caused by H incorporation
212 in B2 FeSi is unusual, because H in the interstitial sites of densely packed metal alloys typically
213 results in a volume increase (Badding et al., 1991; Kato et al., 2020).

214 In our DFT calculations, we first attempted interstitial site substitutions at the face centers of
215 a B2 unit cell (Figure S4b). The site has a distorted octahedral shape. For B2 FeSiH, we found
216 0.6–0.8% unit-cell volume increase, which does not explain our experimental observations
217 (Figure 5c). We, then, hypothesize that H atoms replace equal number of both Fe and Si atoms in
218 the B2 structure (Figure 5f). To maintain the size of the cell within computational reasonable
219 level, we conducted DFT calculations on two configurations: B2-structured Fe₇Si₈H and Fe₈Si₇H
220 for Fe₁₅Si₁₅H₂. DFT calculations show that both Fe₇Si₈H and Fe₈Si₇H configurations decrease the
221 unit-cell volume from that of H-free B2 FeSi to a similar level of our experimental observations
222 (Figure 5c-d). We also found that the energy difference between Fe₇Si₈H and Fe₈Si₇H
223 configurations is small. If unequal numbers of Fe and Si atoms were replaced, some extra Fe
224 metal or Si phases should have existed. However, none of these phases was observed in our XRD
225 and chemical mappings (Figures 2 and 3), which provide supports for the assumption of
226 replacement of equal Fe and Si. We note that although such a mechanism of H replacing Fe/Si in

227 B2 FeSi can well explain our experimental observations, we do not necessarily rule out other
228 possibilities. For instance, Fukai et al. (2001, 2003) proposed that the Fe-H alloys can form
229 superabundant vacancies under high P - T conditions, which could also cause a volume change.

230 In a H-free system, Fischer et al. (2014) documented a boundary between the B20 + B2
231 mixture and B2 structure at ~ 42 GPa. With H, our results show that the stability of the H-alloyed
232 B20 FeSi phase extends at least up to 46.1 GPa and 3500 K (Figure 6). That is, adding H into the
233 FeSi alloy shifts the boundary to a higher pressure (46.1–53 GPa). The pressure comparison is
234 likely robust as the Au pressure calibrant in this study is consistent with that of KBr used by
235 Fischer et al. (2014). The expanded stability of B20 relative to B2 is consistent with the fact that
236 B20 can store more H than B2 as found in this study. We note that the estimated H contents in
237 FeSi alloys are for the quenched solid phases after full reaction with H close to or above melting.
238 Temperature could further change the H solubility in FeSi alloy phases (Tagawa et al., 2021;
239 Okuchi, 1997).

240 **IMPLICATIONS**

241 Our findings of a low H content in solid FeSi alloy phases make an important contrast with
242 Fe metal where high H solubility has been found (Badding et al., 1991), and thus, can affect our
243 understandings on the structure and the dynamics of the planetary cores. Many experiments have
244 been performed to understand H partitioning between silicate melt and Fe metal liquid (Okuchi,
245 1997; Clesi et al., 2018; Tagawa et al., 2021). However, the H partitioning behavior remains
246 controversial among different studies (Okuchi, 1997; Clesi et al., 2018; Tagawa et al., 2021),
247 likely because of impacts from different experimental methods and H sources. In addition,
248 because H can escape from the high-pressure FeH_x phases during decompression to ambient
249 conditions where bcc Fe metal is stable (Okuchi, 1997; Badding et al., 1991), literature results

250 may be biased if the quantification of H in the metal was performed on the recovered samples
251 (Okuchi, 1997; Clesi et al., 2018; Tagawa et al., 2021). We found that the unit-cell volume of
252 synthesized B20 FeSiH_x remains expanded even at 1 bar. Therefore, H likely remains in the
253 crystal structure of the recovered FeSi sample. This stabilizing effect of Si for H can open up a
254 possibility for accurate measurements of H partitioned into Fe-Si alloys using mass spectrometry.

255 Tagawa et al. (2021) recently reported that 0.3–0.6 wt% H could partition into liquid Fe
256 alloys while the metal melt coexists with silicate melt at the early Earth's magma ocean. Some of
257 our heating were performed to temperatures above the melting of FeSi and the pressure range
258 overlaps with the conditions expected in the deep magma ocean (Figure 6). Even for those data
259 points with full reaction with H, we found low H solubility in the temperature quenched solid
260 FeSi alloy (less than 0.3 wt%). Although some H could escape from FeSi during crystallization,
261 we predict that the Si content in Fe alloy liquid of an early magma ocean could limit the amount
262 of H entering the core.

263 The effect of H on the elastic properties of Fe-Si alloys can further help us decipher the
264 abundance of light elements in the planetary cores in the solar system and the exo-planetary
265 systems. Here, we calculated the density and the bulk sound speed (V_{Φ}) of H-bearing B20 and B2
266 phases and compare them with those of Fe metal and Fe_{0.88}Si_{0.12} alloys (6.5 wt% Si) using
267 literature data (Figure 7) (Dewaele et al., 2006; Pepin et al., 2014; Tagawa et al., 2016; Fischer et
268 al., 2014). Note that these experimental results on Fe, FeH, Fe_{0.88}Si_{0.12}, and Fe_{0.88}Si_{0.12}H_x are all
269 documented for 300 K while our DFT results are calculated at essentially 0 K. The temperature
270 impact could be reduced by calculating variations from the respective H-free cases (Figure 7c-d).
271 In this case, we assume that the effect of light elements on the thermal properties of Fe alloys is
272 small. We make a comparison for H/(Fe+Si) = 0.05 in these alloys (~0.1 wt% H), assuming a

273 linear dependence of these properties with respect to the H content. We found that H decreases
274 density and increases V_{ϕ} for the Fe alloys considered. For both density and V_{ϕ} , the magnitudes of
275 H effect are distinct for B2 compared with B20 FeSi, hcp-Fe_{0.88}Si_{0.12}, and hcp-Fe metal (Dewaele
276 et al., 2006; Pepin et al., 2014; Tagawa et al., 2016; Fischer et al., 2014). We note that H is
277 incorporated into interstitial sites for hcp Fe, hcp Fe_{0.88}Si_{0.12}, and B20 FeSi. Here, we attribute the
278 distinct impact of H on density and V_{ϕ} of B2 FeSi to the atomic-scale incorporation mechanism
279 of H as discussed early.

280 Finally, in this study we demonstrated that heating of planetary materials to very high
281 temperature in a pure H medium became feasible using pulsed laser heating in DAC. Many data
282 points in this study were obtained for heating over 2000 K, which is about 300–1000 K higher
283 than the reported melting of FeH (Sakamaki et al., 2009). The highest temperature at 42.6–46.1
284 GPa is 3500K, which is above the melting of FeSi (Figure 6) (Fischer et al., 2014), allowing full
285 reaction between FeSi and H. Although detection of diffuse scattering remains difficult in XRD
286 when combined with pulsed laser heating, it is feasible that the P - T conditions expected for the
287 outer core can be achieved for H-bearing Fe alloys in the future studies using similar
288 experimental configurations.

289 ACKNOWLEDGEMENTS

290 The authors thank A. Wittmann for his assistance on electron microprobe analyses of the
291 recovered samples. This work is supported by NSF-Astronomical Science (AST200567) and
292 NSF-Earth Science (EAR1921298). We acknowledge the support of GeoSoilEnviroCARS
293 (University of Chicago, Sector 13) for synchrotron experiments. GeoSoilEnviroCARS was
294 supported by the National Science Foundation - Earth Sciences (EAR-1634415). This research
295 used resources of the Advanced Photon Source, a U.S. Department of Energy (DOE) Office of

296 Science User Facility operated for the DOE Office of Science by Argonne National Laboratory
297 under Contract No. DE-AC02-06CH11357.

298 **References**

299 Al-Sharif, A., Abu-Jafar, M., and Qteish, A. Structural and electronic structure properties of FeSi:
300 the driving force behind the stability of the B20 phase. *Journal of Physics: Condensed Matter*,
301 13(12):2807, 2001.

302 Anders, E. and Grevesse, N. Abundances of the elements: Meteoritic and solar. *Geochimica et*
303 *Cosmochimica acta*, 53(1):197–214, 1989.

304 Badding, J., Hemley, R., and Mao, H. High-pressure chemistry of hydrogen in metals: In situ
305 study of iron hydride. *Science*, 253(5018):421–424, 1991.

306 Batalha, N. M., Borucki, W. J., Bryson, S. T., Buchhave, L. A., Caldwell, D. A.,
307 ChristensenDalsgaard, J., Ciardi, D., Dunham, E. W., Fressin, F., Gautier III, T. N., et al.
308 Kepler's first rocky planet: -10b. *The Astrophysical Journal*, 729(1):27, 2011.

309 Blochl, P. E. Projector augmented-wave method. *Physical review B*, 50(24):17953, 1994.

310 Caracas, R. and Wentzcovitch, R. Equation of state and elasticity of fesi. *Geophysical Research*
311 *Letters*, 31(20), 2004.

312 Ceperley, D. M. and Alder, B. J. Ground state of the electron gas by a stochastic method.
313 *Physical review letters*, 45(7):566, 1980.

314 Clesi, V., Bouhifd, M. A., Bolfan-Casanova, N., Manthilake, G., Schiavi, F., Raepsaet, C.,
315 Bureau, H., Khodja, H., and Andrault, D. Low hydrogen contents in the cores of terrestrial
316 planets. *Science advances*, 4(3):e1701876, 2018.

- 317 Dewaele, A., Loubeyre, P., Occelli, F., Mezouar, M., Dorogokupets, P. I., and Torrent, M.
318 Quasihydrostatic equation of state of iron above 2 Mbar. *Physical Review Letters*, 97(21):
319 215504, 2006.
- 320 Fischer, R. A., Campbell, A. J., Reaman, D. M., Miller, N. A., Heinz, D. L., Dera, P., and
321 Prakapenka, V. B. Phase relations in the Fe–FeSi system at high pressures and temperatures.
322 *Earth and Planetary Science Letters*, 373:54–64, 2013.
- 323 Fischer, R. A., Campbell, A. J., Caracas, R., Reaman, D. M., Heinz, D. L., Dera, P., and
324 Prakapenka, V. B. Equations of state in the Fe-FeSi system at high pressures and temperatures.
325 *Journal of Geophysical Research: Solid Earth*, 119(4):2810–2827, 2014.
- 326 Fukai, Y. Some properties of the Fe-H system at high pressures and temperatures, and their
327 implications for the Earth’s core. *High Pressure Research: Application to Earth and Planetary*
328 *Sciences*, pages 373–385, 1992.
- 329 Fukai, Y., Haraguchi, T., Hayashi, E., Ishii, Y., Kurokawa, Y., and Yanagawa, J.
330 Hydrogeninduced superabundant vacancies and diffusion enhancement in some fcc metals. In
331 *Defect and Diffusion Forum*, volume 194, pages 1063–1068. Trans Tech Publ, 2001.
- 332 Fukai, Y., Mori, K., and Shinomiya, H. The phase diagram and superabundant vacancy formation
333 in fe–h alloys under high hydrogen pressures. *Journal of alloys and compounds*, 348(1-2):105–
334 109, 2003.
- 335 Goncharov, A. F., Prakapenka, V. B., Struzhkin, V. V., Kantor, I., Rivers, M. L., and Dalton, D.
336 A. X-ray diffraction in the pulsed laser heated diamond anvil cell. *Review of Scientific*
337 *Instruments*, 81(11):113902, 2010.

- 338 Grevesse, N. and Sauval, A. Standard solar composition. *Space Science Reviews*, 85(1): 161–174,
339 1998.
- 340 Hirose, K., Labrosse, S., and Hernlund, J. Composition and state of the core. *Annual Review of*
341 *Earth and Planetary Sciences*, 41:657–691, 2013.
- 342 Jontof-Hutter, D., Rowe, J. F., Lissauer, J. J., Fabrycky, D. C., and Ford, E. B. The mass of the
343 mars-sized exoplanet -138 b from transit timing. *Nature*, 522(7556):321–323, 2015.
- 344 Kato, C., Umemoto, K., Ohta, K., Tagawa, S., Hirose, K., and Ohishi, Y. Stability of fcc phase
345 FeH to 137 GPa. *American Mineralogist: Journal of Earth and Planetary Materials*,
346 105(6):917–921, 2020.
- 347 Knibbe, J. S. and van Westrenen, W. The thermal evolution of mercury’s fe–si core. *Earth and*
348 *Planetary Science Letters*, 482:147–159, 2018.
- 349 Li, J. and Fei, Y. Experimental constraints on core composition. *Treatise on geochemistry*, 2:568,
350 2003.
- 351 Lin, J.-F., Campbell, A. J., Heinz, D. L., and Shen, G. Static compression of iron-silicon alloys:
352 Implications for silicon in the Earth’s core. *Journal of Geophysical Research: Solid Earth*,
353 108(B1), 2003.
- 354 Machida, A., Saitoh, H., Sugimoto, H., Hattori, T., Sano-Furukawa, A., Endo, N., Katayama, Y.,
355 Iizuka, R., Sato, T., Matsuo, M., et al. Site occupancy of interstitial deuterium atoms in face-
356 centred cubic iron. *Nature communications*, 5(1):1–6, 2014.
- 357 Moroni, E., Wolf, W., Hafner, J., and Podloucky, R. Cohesive, structural, and electronic
358 properties of Fe-Si compounds. *Physical Review B*, 59(20):12860, 1999.

- 359 Mortensen, J. J., Hansen, L. B., and Jacobsen, K. W. Real-space grid implementation of the
360 projector augmented wave method. *Physical Review B*, 71(3):035109, 2005.
- 361 Nittler, L. R., Starr, R. D., Weider, S. Z., McCoy, T. J., Boynton, W. V., Ebel, D. S., Ernst, C. M.,
362 Evans, L. G., Goldsten, J. O., Hamara, D. K., et al. The major-element composition of
363 mercury's surface from messenger x-ray spectrometry. *Science*, 333(6051): 1847–1850, 2011.
- 364 Okuchi, T. Hydrogen partitioning into molten iron at high pressure: implications for Earth's core.
365 *Science*, 278(5344):1781–1784, 1997.
- 366 P'epin, C. M., Dewaele, A., Geneste, G., Loubeyre, P., and Mezouar, M. New iron hydrides
367 under high pressure. *Physical review letters*, 113(26):265504, 2014.
- 368 P'epin, C. M., Geneste, G., Dewaele, A., Mezouar, M., and Loubeyre, P. Synthesis of FeH₅: A
369 layered structure with atomic hydrogen slabs. *Science*, 357(6349):382–385, 2017.
- 370 Perdew, J. P., Burke, K., and Ernzerhof, M. Generalized gradient approximation made simple.
371 *Physical review letters*, 77(18):3865, 1996.
- 372 Piet, H., Leinenweber, K., Greenberg, E., Prakapenka, V. B., and Shim, S.-H. Effects of
373 hydrogen on the phase relations in Fe–FeS at pressures of Mars-sized bodies. *Journal of*
374 *Geophysical Research: Planets*, page e2021JE006942, 2021.
- 375 Sakamaki, K., Takahashi, E., Nakajima, Y., Nishihara, Y., Funakoshi, K., Suzuki, T., and Fukai,
376 Y. Melting phase relation of FeH_x up to 20 GPa: Implication for the temperature of the Earth's
377 core. *Physics of the Earth and Planetary Interiors*, 174(1-4):192–201, 2009.
- 378 Sata, N., Hirose, K., Shen, G., Nakajima, Y., Ohishi, Y., and Hirao, N. Compression of FeSi,
379 Fe₃C, Fe_{0.95}O, and FeS under the core pressures and implication for light element in the
380 Earth's core. *Journal of Geophysical Research: Solid Earth*, 115(B9), 2010.

- 381 Shahar, A., Driscoll, P., Weinberger, A., and Cody, G. What makes a planet habitable? *Science*,
382 364(6439):434–435, 2019.
- 383 Shim, S. PeakPo - a python software for x-ray diffraction analysis at high pressure and high
384 temperature. Zenodo: Meyrin, Switzerland, 2017.
- 385 Smith, J. M. Introduction to chemical engineering thermodynamics, 1950.
- 386 Stevenson, D. J. Planetary magnetic fields. *Earth and planetary science letters*, 208(1-2): 1–11,
387 2003.
- 388 Tagawa, S., Ohta, K., Hirose, K., Kato, C., and Ohishi, Y. Compression of Fe–Si–H alloys to
389 core pressures. *Geophysical Research Letters*, 43(8):3686–3692, 2016.
- 390 Tagawa, S., Sakamoto, N., Hirose, K., Yokoo, S., Hernlund, J., Ohishi, Y., and Yurimoto, H.
391 Experimental evidence for hydrogen incorporation into earth’s core. *Nature communications*,
392 12(1):1–8, 2021.
- 393 Terasaki, H., Shibasaki, Y., Sakamaki, T., Tateyama, R., Ohtani, E., Funakoshi, K.-i., and Higo,
394 Y. Hydrogenation of fesi under high pressure. *American Mineralogist*, 96(1):93–99, 2011.
- 395 Vocadlo, L., Price, G. D., and Wood, I. Crystal structure, compressibility and possible phase
396 transitions in ϵ -FeSi studied by first-principles pseudopotential calculations. *Acta*
397 *Crystallographica Section B: Structural Science*, 55(4):484–493, 1999.
- 398 Ye, Y., Shim, S.-H., Prakapenka, V., and Meng, Y. Equation of state of solid ne intercalibrated
399 with the mgo, au, pt, nacl-b2, and ruby pressure scales up to 130 gpa. *High Pressure Research*,
400 38(4):377–395, 2018.

- 401 Zhang, G., Yukawa, H., Watanabe, N., Saito, Y., Fukaya, H., Morinaga, M., Nambu, T., and
402 Matsumoto, Y. Analysis of hydrogen diffusion coefficient during hydrogen permeation
403 through pure niobium. *International journal of hydrogen energy*, 33(16):4419–4423, 2008.
- 404 Zhao, K., Jiang, G., and Wang, L. Electronic and thermodynamic properties of B2-FeSi from first
405 principles. *Physica B: Condensed Matter*, 406(3):363–367, 2011.
- 406

407 **List of figure captions:**

408 **Figure 1:** Laser heating of FeSi in a H medium at high *P-T*. (a) A schematic diagram of a DAC
409 loaded with the FeSi sample foil in H. The foil was made by cold compressing FeSi powder (an
410 average grain size of $\sim 1\mu\text{m}$) to an initial thickness of 5–10 μm . The H gas likely penetrates the
411 sample foil and exists around the grain boundaries. (b) and (c) Images of the sample in a
412 diamond-anvil cell at 61.9 GPa and 300 K taken before and after laser heating up to 2200 K,
413 respectively. The circles highlight the heated area. The white spots in (b) are from the sample
414 migration by melting at high temperatures.

415 **Figure 2:** Two-dimensional XRD mapping of the heated region at 46.1 GPa and 300 K. (a) XRD
416 patterns measured after heating up to 3500 K at 46.1 GPa. The patterns from top to bottom were
417 collected from the heated center to the edge of the hot spot within an $8\times 8\mu\text{m}^2$ area with a 2 μm
418 step. The B2 structure is dominant with some weak peaks from B20. The Miller indices of the
419 B20 and B2 phases are presented in the blue and red labels, respectively. No additional peaks
420 were found in any of the heated area, suggesting no new phases other than B2 and B20 exist after
421 laser heating. The wavelength of the incident X-ray is 0.3344 \AA . (b) A 2D map of the unit-cell
422 volumes of the synthesized B2 phase at 46.1 GPa and 300 K. A small volume difference (0.4%)
423 indicates that the synthesized products are homogeneous over the heated region.

424 **Figure 3:** Electron probe micro analyzer measurements on the recovered FeSi sample from 61.9
425 GPa and 2200 K. (a) A back-scattered electron image. Spots A and B are heated and unheated
426 areas, respectively. (b) and (c) Energy-dispersive spectroscopy maps of Fe and Si, respectively.
427 (d) Quantitative measurements for the chemical compositions of spots A and B in (a). We found
428 little changes in the Fe and Si contents of the sample after heating. The changed unit-cell

429 volumes of B20 and B2 in the heated spot detected from XRD (refer to Figures 4-5) provide
430 strong evidence on the incorporation of H into the crystal structure of FeSi.

431 **Figure 4:** (a) X-ray diffraction patterns at *in situ* high *P-T*. At 30.1 GPa and 2385 K, B20 is the
432 main phase (the blue ticks) and a weak peak of the B2 (the red ticks) phase appear. With a
433 pressure increase to 42.6 GPa, heating up to 2600 K results in a conversion to the B2 structure,
434 which coexists with the weak B20 structure. At 61.9 GPa and 2160 K, the B20 structure
435 completely transforms into the B2 structure. (b) Diffraction patterns of the recovered FeSiH_x at
436 ambient conditions, compared with H-free FeSi. FeSiH_x shows larger *d*-spacings than the H-free
437 FeSi alloys as highlighted in the inset which is a zoom-in view of the gray rectangular area. The
438 wavelength of incident X-ray is 0.3344 Å.

439 **Figure 5:** The volumes of the synthesized (a and b) B20 and (c and d) B2 FeSiH_x phases. The
440 volumes per atoms are shown in (a) and (c), and the volume changes (ΔV) due to H
441 incorporation are shown in (b) and (d). ΔV is the difference between the measured volumes of H-
442 bearing FeSiH_x and H-free FeSi (Fischer et al., 2014; Lin et al., 2003). The legend in (d) is shared
443 for (a)-(d), showing different heating conditions in this study. The open and solid symbols are
444 decompression and compression data, respectively. The thin black curves are for H-free FeSi
445 (Lin et al., 2003; Fischer et al., 2014). The thick curves are for the DFT-GGA calculations for H-
446 bearing FeSiH_x alloy phases with the labeled compositions. We show crystal structure models for
447 the H alloying with (e) B20 and (f) B2 FeSi. For B20, H occupies the interstitial sites at the cubic
448 center to form FeSiH_{0.25}, where only a quarter of the sites in a unit cell are occupied. For the
449 slight volume decrease found in B2, instead of interstitial sites, H may replace one Fe and one Si
450 atoms to form Fe₁₅Si₁₅H₂. The substitution mechanism was modeled with two separate

451 configurations of $2 \times 2 \times 2$ cells of $\text{Fe}_7\text{Si}_8\text{H}$ and $\text{Fe}_8\text{Si}_7\text{H}$. The estimated uncertainties of pressures
452 and volumes are shown but they are in general smaller than the size of symbols.

453 **Figure 6:** Observations of stable FeSiH_x phases at high P - T . The solid purple and red circles
454 represent coexistence of B2 and B20 phases and pure B2 phase, respectively. The solid black line
455 indicates the estimated phase boundary of synthesized H-bearing FeSiH_x alloys. The dashed black
456 lines are the melting curve and the phase boundary of stoichiometric FeSi (Fischer et al., 2014).

457 **Figure 7:** Modeled thermoelastic properties of H-bearing (solid curves) and H-free (dashed
458 curves) FeSi alloys at high pressures and essentially 0 K. (a) and (b) Density and bulk sound
459 velocity, respectively. (c) and (d) Variations of density and bulk sound velocity of FeSiH_x phases
460 by $x = 0.1$ or $\text{H}/(\text{Fe}+\text{Si}) = 0.05$ compared to H-free cases. Properties of B20 and B2 phases are
461 obtained from our GGA calculations. We compare these results with hcp Fe (Dewaele et al.,
462 2006), dhcp FeH (Pepin et al., 2014), hcp $\text{Fe}_{0.88}\text{Si}_{0.12}$ and hcp $\text{Fe}_{0.88}\text{Si}_{0.12}\text{H}_{0.79}$ (Tagawa et al., 2016).

463

464

465

466

467

468

469

470

471

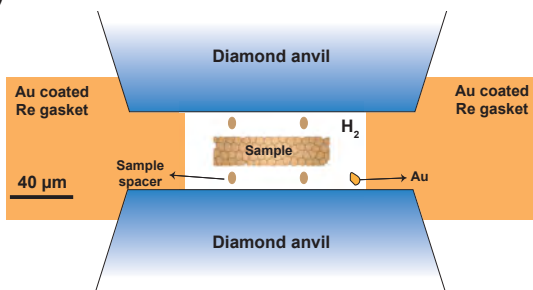
472 **Table 1:** Unit-cell parameters of the B20 and B2 phases synthesized in a H medium at high
473 pressures. These data points were measured during compression or decompression at 300 K. The
474 synthesis P - T conditions are given in the first row of each subsection. Uncertainties on the last
475 digit(s) are shown in parentheses.

Pressure (GPa)	a (Au) (Å)	a (B20) (Å)	a (B2) (Å)	Pressure (GPa)	a (Au) (Å)	a (B20) (Å)	a (B2) (Å)
Unheated (fresh) region, Cold compression				42.6 GPa and 1446-3820 K, Compression			
ambient	-	4.4881(7)	-	42.6(15)	3.8659(10)	4.3200(9)	2.6479(2)
21.4(7)	3.9478(5)	4.3402(6)	-	45.5(12)	3.8564(9)	4.2953(11)	2.6430(2)
31.1(7)	3.9074(5)	4.3002(7)	-	45.8(17)	3.8554(11)	4.2957(12)	2.6422(2)
36.0(9)	3.8891(7)	4.2799(7)	-	46.1 GPa and 1900-3500 K, Decompression			
42.6(9)	3.8659(7)	4.2536(9)	-	46.1(18)	3.8545(12)	4.2977(10)	2.6415(4)
48.1(15)	3.8482(11)	4.2326(10)	-	45.2(30)	3.8573(16)	4.2983(16)	2.6419(4)
50.2(10)	3.8417(8)	4.2122(10)	-	43.6(11)	3.8625(8)	4.3062(18)	2.6453(5)
55.3(9)	3.8268(7)	4.2028(10)	-	38.9(21)	3.8785(12)	4.3227(20)	2.6545(4)
55.4(9)	3.8265(7)	4.2059(10)	-	33.5(26)	3.8982(14)	4.3336(22)	2.6641(3)
57.7(11)	3.8200(9)	4.1935(13)	-	33.7(24)	3.8974(13)	4.3393(30)	2.6640(7)
58.3(18)	3.8183(12)	4.1895(15)	-	31.4(22)	3.9063(12)	4.3499(10)	2.6682(3)
61.8(22)	3.8089(14)	4.1808(14)	-	17.4(8)	3.9684(5)	4.4058(8)	2.7049(3)
66.0(22)	3.8057(13)	4.1755(14)	-	13.1(3)	3.99912(5)	4.4460(8)	2.7284(3)
67.5(20)	3.7941(12)	4.1616(16)	-	8.9(3)	4.0158(2)	4.4724(6)	2.7468(2)
73.5(25)	3.7795(14)	4.1524(22)	-	ambient	-	4.5234(3)	2.7772(2)
21.4 GPa and 1830-2485 K, Compression				53.3 GPa and 1670-2100 K, Compression			
21.4(3)	3.9478(3)	4.3577(4)	-	53.0(10)	3.8334(8)	-	2.6147(4)
26.0(5)	3.9284(4)	4.3400(4)	-	57.5(13)	3.8206(10)	-	2.6071(5)
27.7(6)	3.9212(4)	4.3338(5)	-	57.8(13)	3.8197(10)	-	2.6054(5)
29.1(8)	3.9154(7)	4.3291(6)	-	61.9 GPa and 1700-2160 K, Decompression			
30.1(9)	3.9114(8)	4.3245(6)	-	61.9(14)	3.8086(10)	-	2.5980(6)
30.7(11)	3.9090(9)	4.3227(7)	-	61.9(14)	3.8086(10)	-	2.5964(6)
31.1 GPa and 1409-2650 K, Compression				62.3(15)	3.8075(12)	-	2.5950(7)
31.1(11)	3.9074(8)	4.3312(5)	2.6751(1)	58.3(20)	3.8183(13)	-	2.6015(7)
32.1(14)	3.9035(11)	4.3264(6)	2.6721(1)	58.9(22)	3.8167(13)	-	2.6020(6)
33.9(15)	3.8967(12)	4.3206(6)	2.6688(1)	57.7(26)	3.8200(14)	-	2.6035(6)
35.3(20)	3.8914(14)	4.3154(6)	2.6658(2)	55.4(11)	3.8265(9)	-	2.6060(4)
38.0(22)	3.8817(14)	4.3062(6)	2.6594(2)	48.2(13)	3.8479(10)	-	2.6276(4)
39.7(26)	3.8757(16)	4.2977(7)	2.6555(2)	27.6(15)	3.9216(11)	-	2.6911(3)
41.8(11)	3.8685(8)	4.2896(7)	2.6516(2)	0.3(12)	4.0763(9)	-	2.7750(2)
42.6(13)	3.8659(10)	4.2845(7)	2.6511(2)	ambient	-	-	2.7758(2)

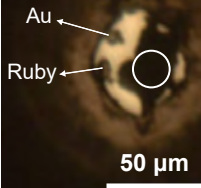
476

Figure 1

(a)



(b) Before heating

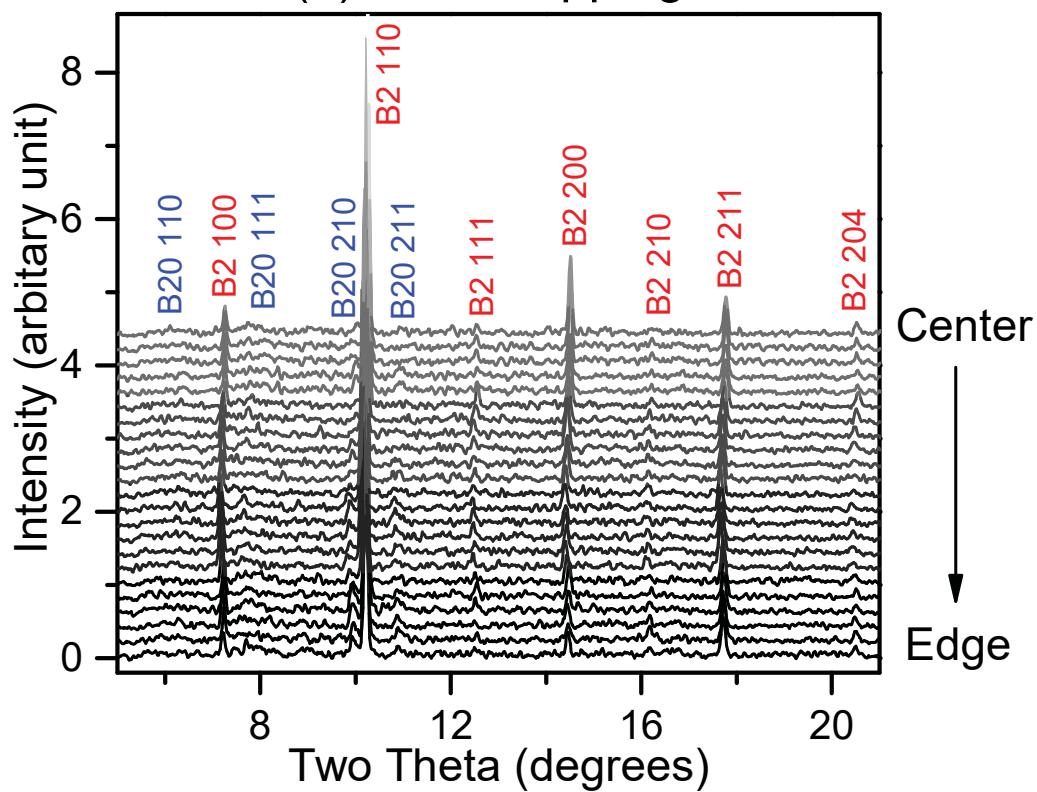


(c) After heating



Figure 2

(a) XRD Mapping



(b) Unit-Cell Volume of B2

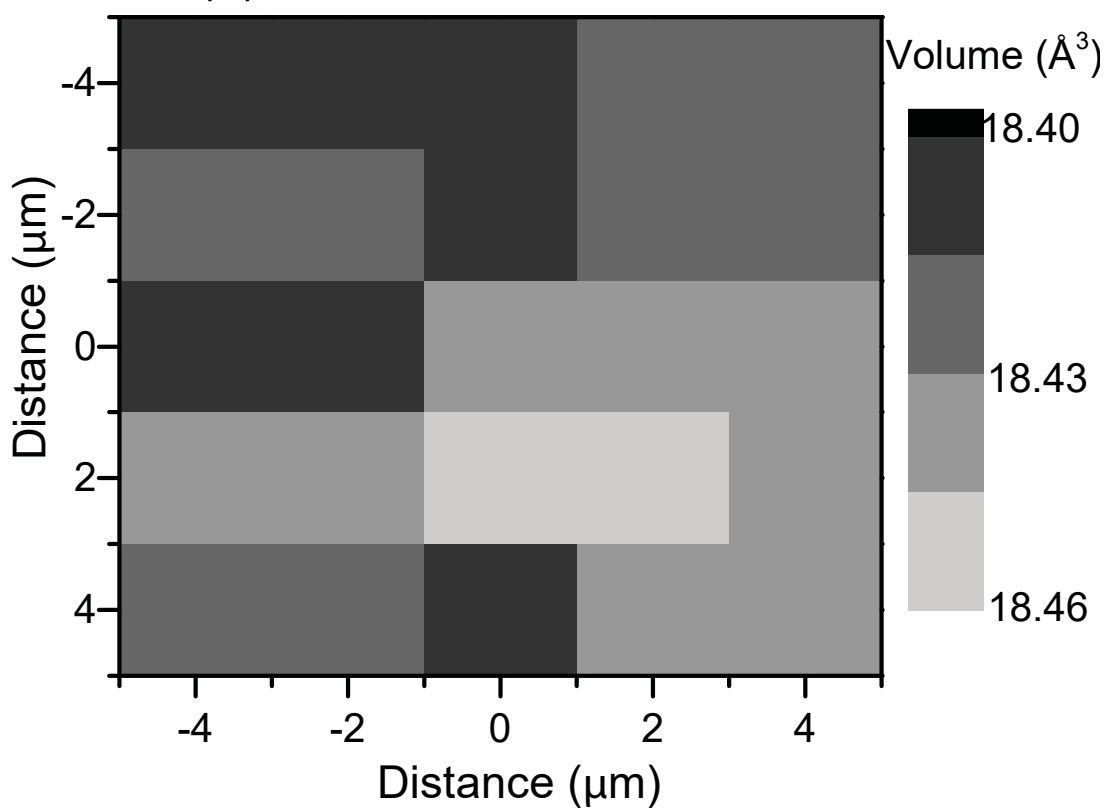


Figure 3

Recovered Sample

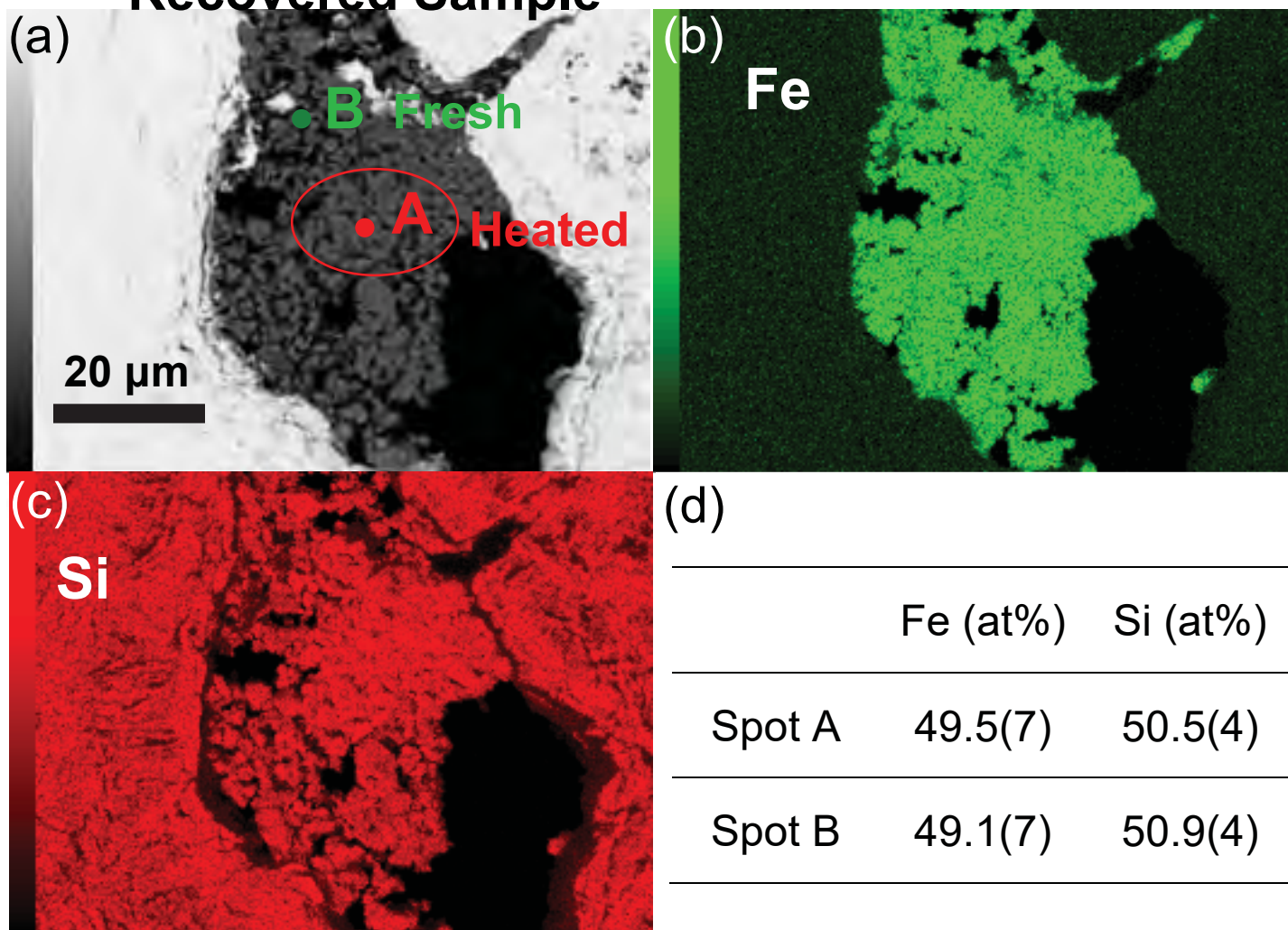


Figure 4

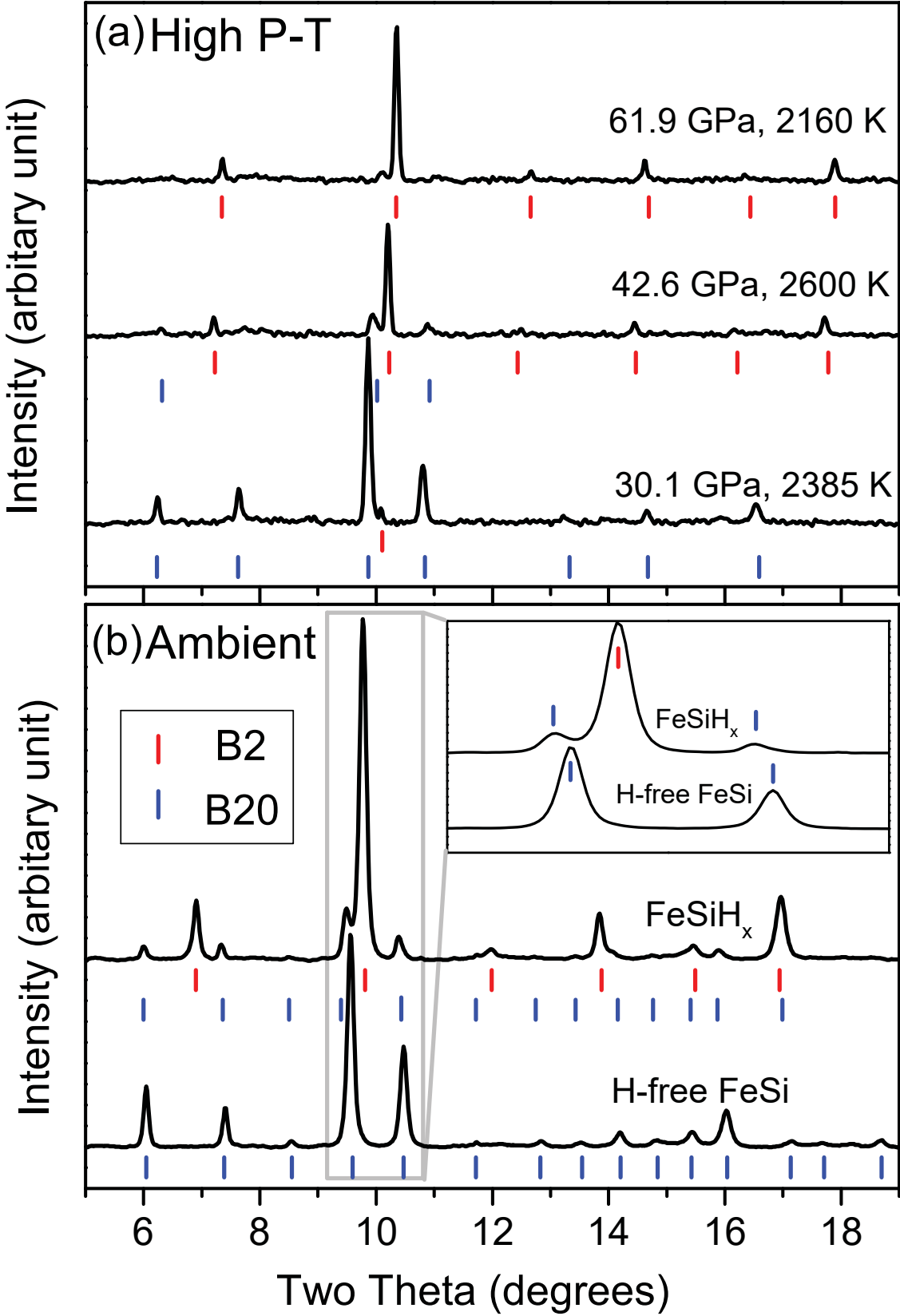


Figure 5

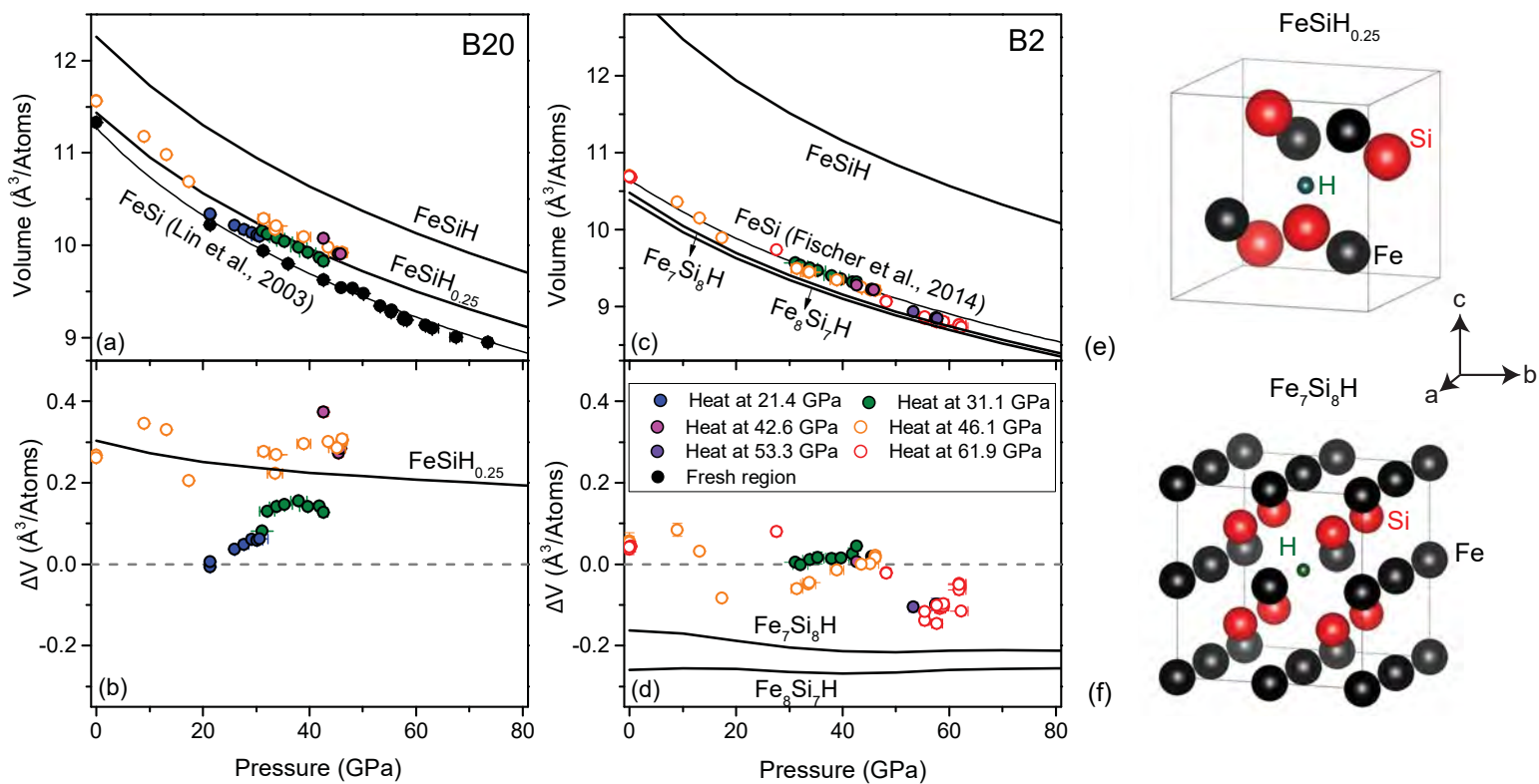


Figure 6

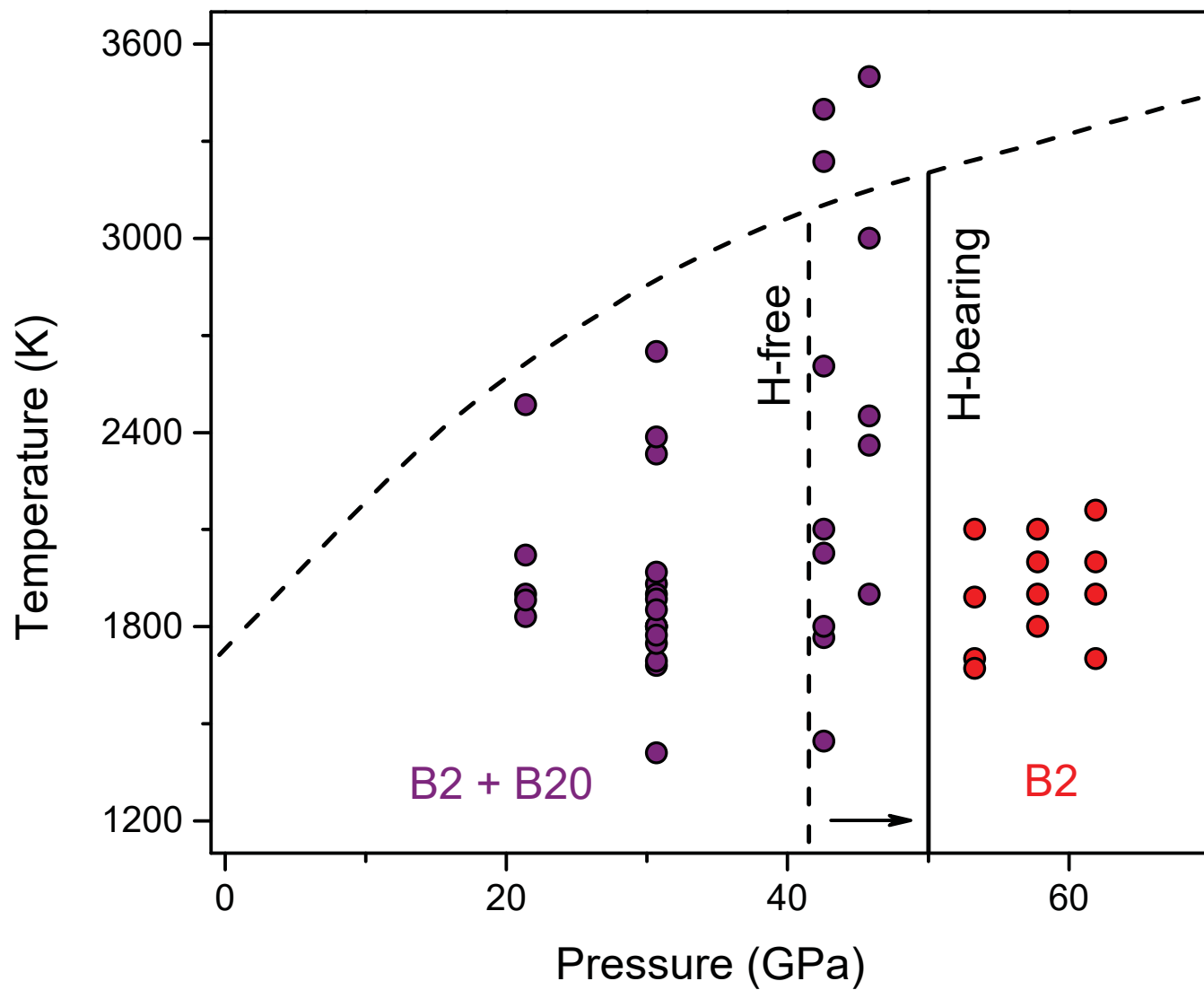


Figure 7

